Biomedical Microdevices (2020) 22: 52
https://doi.org/10.1007/s10544-020-00508-1

Inertial flow focusing: a case study in optimizing cellular trajectory through a microfluidic MEMS device for timing-critical applications

Luke H.C. Patterson[1] · Jennifer L. Walker[1] · Mark A. Naivar[2] · Evelyn Rodriguez-Mesa[2] · Mehran R. Hoonejani[2] · Kevin Shields[2] · John S. Foster[2] · Adele M. Doyle[1,3] · Megan T. Valentine[1,3] · Kimberly L. Foster[1,4]

Published online: 8 August 2020

Abstract

Although microfluidic micro-electromechanical systems (MEMS) are well suited to investigate the effects of mechanical force on large populations of cells, their high-throughput capabilities cannot be fully leveraged without optimizing the experimental conditions of the fluid and particles flowing through them. Parameters such as flow velocity and particle size are known to affect the trajectories of particles in microfluidic systems and have been studied extensively, but the effects of temperature and buffer viscosity are not as well understood. In this paper, we explored the effects of these parameters on the timing of our own cell-impact device, the μHammer, by first tracking the velocity of polystyrene beads through the device and then visualizing the impact of these beads. Through these assays, we find that the timing of our device is sensitive to changes in the ratio of inertial forces to viscous forces that particles experience while traveling through the device. This sensitivity provides a set of parameters that can serve as a robust framework for optimizing device performance under various experimental conditions, without requiring extensive geometric redesigns. Using these tools, we were able to achieve an effective throughput over 360 beads/s with our device, demonstrating the potential of this framework to improve the consistency of microfluidic systems that rely on precise particle trajectories and timing.

Keywords Cell impact · Dynamic cell compression · Microfluidics · MEMS · Inertial focusing · Reynolds number

1 Introduction

The inherently heterogeneous nature of biological cell populations demands robust, high-throughput assays to effectively investigate the consequences of mechanical impacts on cell properties and functions (Desmaële et al. 2011). Although a number of technologies exist to study how impact affects cells (Loh et al. 2009), few do so with the throughput and tunable impact parameters of a microfluidic MEMS device like the μHammer (Patterson et al. 2019). This high strain, high strain rate cell-impact device is fabricated out of single-crystal silicon and has a magnetically actuated Ni–Fe armature in microchip format. It can compress individual cells with adjustable strain magnitude (10% to 90%), strain duration (10 μs to 1000 μs), and high throughput (10,000 to 1,000,000 cells per experiment). Cells of different sizes (5-μm to 16-μm diameter) can be perturbed at different temperatures (4 °C to 37 °C), after which they can be removed from the μHammer for analysis or continued culture.

While flexibility in experimental design offers significant advantages, it also introduces potential complications. In particular, the performance of microfluidic systems like the μHammer can be influenced by the aforementioned changes in temperature (which influences fluid viscosity) and particle size, since the path of cells and other particles flowing through them depends strongly on the ratio of inertial to viscous forces (Asmolov 1999; Di Carlo et al. 2007; Zhang et al. 2016). Maintaining a consistent and reproducible flow of particles is crucial to the performance of many microfluidic devices, including those that perform flow cytometry (Bhagat et al.

✉ Luke H.C. Patterson
lpatterson@ucsb.edu

[1] Department of Mechanical Engineering, University of California, Santa Barbara, CA, USA

[2] Owl biomedical, Santa Barbara, CA, USA

[3] Neuroscience Research Institute, and Center for Bioengineering, University of California, Santa Barbara, CA, USA

[4] Department of Physics and Engineering Physics, and Department of Biomedical Engineering, School of Science and Engineering, Tulane University, New Orleans, LA, USA

2010b; Foster et al. 2018; Oakey et al. 2010; Sun and Morgan 2010), particle filtration and separation (Bhagat et al. 2009; Hur et al. 2011; Masaeli et al. 2012; Ozkumur et al. 2013; Sun and Morgan 2010), cellular mechanotyping (Deng et al. 2017; Gossett et al. 2012), and pathogen detection (Warkiani et al. 2015). Particle trajectories within these systems have been studied extensively as a function of flow velocity, particle size, and to a lesser extent particle concentration in a variety of different channel geometries (Di Carlo et al. 2007; Oakey et al. 2010; Zhang et al. 2016). However, little documentation exists regarding the effects of temperature and buffer viscosity in these systems. Although some have investigated the role of buffer viscosity in mixing and droplet formation (Tice et al. 2004; Wang et al. 2011) or in inertial focusing of viscoelastic fluids and coflow systems (Lee et al. 2018; Leshansky et al. 2007), this work seeks to more deeply understand how the interplay between buffer fluid temperature, viscosity, and other experimental parameters affects the inertial focusing and performance of a microfluidic device with a single stream of Newtonian fluid.

To explore this relationship, we characterized the impact and focusing profiles of polystyrene beads flowing through the μHammer. We assessed these profiles as a function of temperature, viscosity, flow velocity, particle size, and particle concentration in order to develop a robust understanding of how these parameters affect our device. By doing so, we gain the tools to optimize the μHammer's performance under a variety of different experimental conditions, which can ultimately serve as a framework for the design and optimization of other microfluidic devices.

2 Background and methods

2.1 Experimental overview

The design and operation of the μHammer is described in detail in our previous work (Patterson et al. 2019). Briefly, biological cells (or any other desired type of particles) are suspended in Tyto® Running Buffer (Miltenyi Biotec, Germany) and loaded into a macroscale cartridge that interfaces the device with the MACSQuant® Tyto® system (designed by Owl biomedical, USA; manufactured by Miltenyi Biotec, Germany). Prior to entering the μHammer chip, each individual particle is pressure-driven through a focusing channel that has a variable cross-section as described by Foster et al. (2018) (see Sections 2.2 and 2.3 for further description of flow focusing). It then flows into and through the μHammer channel, where the particle is eventually sensed by two laser-detector pairs spaced 50 μm apart. These detectors measure either fluorescence or the backscatter signal that arises from reflection as the particle passes through the laser planes. The transit time between these lasers, t_{LL}, is measured and used to calculate the particle velocity, u (see Table 1 and Fig. 1 for further explanations and illustrations of all timing parameters). The flow is controlled such that the average t_{LL} of the particle population is set to a user-specified value.

In this work, two average particle velocities are compared: "slow" velocity, u_S (1.2 to 1.3 m/s, $\overline{t_{LL}}$ = 40 μs), and "fast" velocity, u_F (2.3 to 2.7 m/s, $\overline{t_{LL}}$ = 20 μs). These velocities represent those typically used when operating the MACSQuant® Tyto® system for cell-sorting applications. The calculated particle velocity is used to predict the particle arrival time at the center of the μHammer face, t_{DA}, measured in relation to the time of detection by the final laser, t_D. This particle arrival time depends on the distance between the detecting laser and the center of the μHammer impact face, x_{LH}. To actuate the μHammer, an external solenoid is activated t_{DS} microseconds after particle detection at a predetermined amount of time before the particle is expected to arrive at the μHammer face, t_{SA}. The μHammer then completes actuation t_{SC} microseconds after the solenoid is actuated. To account for slight differences in t_{SC} between devices (±1 μs), we define our timing settings in terms of the pre-arrival closure time, t_{AC}. This value measures the amount of time after the particle is predicted to arrive at the center of the impact face that the μHammer completes actuation. When full actuation is reached, the amount of compression applied to each particle depends on the final gap distance, x_G, which is determined by the length of the pincers bounding the impact face. The particles are held in compression for a user-specified period, after which they are released and the μHammer returns to rest in preparation for the next actuation.

2.2 Theoretical background for flow focusing

When cells and other particles pass through a microfluidic channel, they experience both inertial and viscous drag forces, the ratio of which is typically described by the Reynold's number, *Re*. Under certain conditions, this combination of forces pushes the particles away from the center of the channel toward equilibrium points near the periphery. The conditions under which particles are guided into these equilibrium positions in straight channels is described by the particle Reynolds number, Re_p (Asmolov 1999; Di Carlo et al. 2007). This quantity is related to the Reynolds number of the flow, *Re*, but is rescaled to account for the ratio of particle to channel size:

$$Re_p = \frac{u_{max}\rho a^2}{\mu D_h}.$$

In this relationship, u_{max} = maximum fluid velocity, ρ = fluid density, a = particle diameter, μ = dynamic fluid viscosity, and D_h = channel hydraulic diameter, which is a function of the channel height, h, and width, w: $D_h = 2hw / (h + w)$. When Re_p is on the order of 1, inertial lift forces dominate and the

Table 1 μHammer experimental variables

Category	Variable	Parameter described	Definition
Setup	x_G	Final gap distance	Distance between impact face and upper channel wall after actuation (fixed device parameter)
	x_{HF}	Hammer face width	Distance between pincers that bound impact face (fixed device parameter)
	x_{LH}	Laser-hammer separation distance	Distance between detecting laser and center of impact face (adjustable)
	x_{LL}	Intra-laser separation distance	Distance between detecting lasers (fixed device parameter)
Flow	t_B / t_V	Blue / violet laser detection time	Time that particle signal pulse is detected by blue (488 nm) and violet (405 nm) laser detector
	t_D	Detection time	Time that particle signal pulse is detected by final laser detector ($t_D = t_V$)
	t_{LL}	Intra-laser transit time	Time of transit between blue and violet lasers ($t_{LL} = t_V - t_B$)
	u	Particle velocity	Velocity of particle as detected by lasers ($u = x_{LL} / t_{LL}$)
Timing	t_{DS}	Solenoid trigger time	Time after particle detection that solenoid pulse triggers actuation ($t_{DA} - t_{SA}$)
	t_{DA}	Particle arrival time	Time after detection that particle is predicted to arrive at center of impact face ($t_{LL} \cdot x_{LH} / x_{LL}$)
	t_{SA}	Pre-arrival trigger time	Time before particle is predicted to arrive at μHammer that solenoid triggers actuation ($t_{SC} - t_{AC}$)
	t_{SC}	μHammer closure time	Time after solenoid trigger that μHammer fully actuates (varies between devices)
	t_{AC}	Post-arrival closure time	Time after particle is predicted to arrive at μHammer that it fully actuates ($t_{DS} + t_{SC} - t_{DA}$)
	t_{SD}	Post-trigger detection time	Time after solenoid trigger that next particle is detected (varies with distance between cells)
	x_C	Particle-center separation distance	Distance of impacted particle from center of impact face (varies based on accuracy of timing)
	ω_{eff}	Effective impact frequency	Frequency of centered particle impacts by μHammer (varies with x_C of particle population)

particles are focused to equilibrium positions that depend on the channel geometry (Di Carlo et al. 2007). In the case of a rectangular channel as is used in the μHammer, there are generally two equilibrium positions that are centered along the longest sides of the channel (Fig. 2a). The width of these streams as well as their distance from the channel wall, x_f, can vary with the Re_p value of the system (Di Carlo et al. 2007). In order for particles to reach their equilibrium positions,

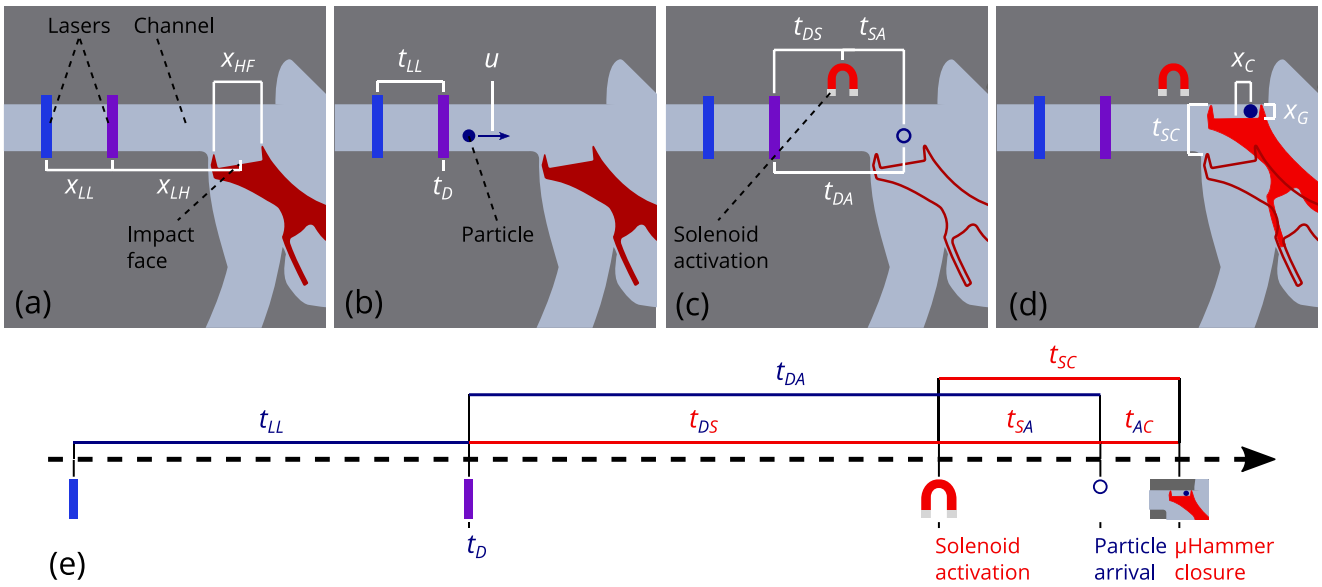

Fig. 1 Illustrations of μHammer experimental variables from Table 1 overlaid on μHammer schematic as viewed from top of device. **a** Variables that define device dimensions related to experimental setup. Blue and violet laser-interrogation positions marked, along with channel and center of impact face. **b** Variables related to flow. Particle depicted travelling through channel. **c** Variables related to timing. Red magnet illustrates activation of external solenoid (not shown). Outlines of μHammer (dark red outline) and bead (dark blue outline) depict their predicted locations in the absence of device actuation. See Fig. 6b inset for illustration of t_{SD}. **d** Variables relating to μHammer actuation and cell impact. μHammer before actuation depicted in dark red outline, μHammer at full actuation depicted in solid red. **e** Overall sequence of timing variables. Movement from left to right depicts the passage of time. Timing variables associated with the bead are depicted in dark blue, while variables associated with the solenoid activation and μHammer actuation are depicted in red

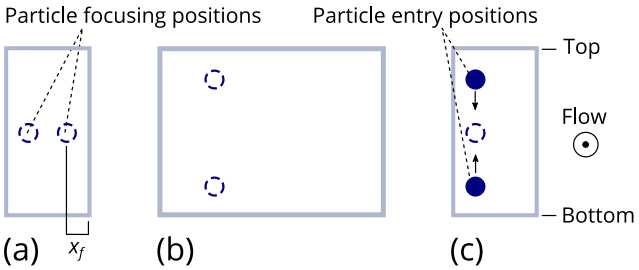

Fig. 2 Illustrations of focused stream positions for different channel geometries and experimental conditions. In all panels, channel cross-section is depicted in grey, with flow coming out of page. Top and bottom of channels are marked. Focused stream locations at equilibrium are depicted by blue dashed circles. **a** Stream positions for generic rectangular channel (height / width ratio $h / w > 1$). Distance of focused stream from the closest channel wall, x_f, is marked. Stream width is determined by size of focused particle region(s). **b** Stream positions for inlet focusing channel (single slice of variable cross-section geometry shown; $h / w = 0.75$). **c** Stream positions for μHammer channel ($h / w = 2$). Particle positions at channel entry are marked with solid blue circles. Arrows depict movement of particles toward focusing position. Only one equilibrium position is shown, since particles are already ordered when they enter the channel and thus do not sample the second focusing node depicted in panel a

however, they must travel a minimum distance along the channel length, L, which we define as:

$$L_{min} = \frac{3\pi\mu h^3}{u_{max}\rho a^3}$$

(Bhagat et al. 2009). The concentration of particles suspended in the buffer solution also affects their trajectories, since when particles are too close together they fail to focus effectively into their preferred streamlines due to steric crowding effects (Di Carlo 2009; Reece and Oakey 2016; Wang et al. 2015). The critical volume fraction of particles for the onset of this effect, φ_C, is approximately 0.001 to 0.01 (Di Carlo 2009; Humphry et al. 2010; Kahkeshani et al. 2016). On the other hand, for $\varphi < \varphi_C$, some studies have reported that focused streams form more quickly and to a narrower width as φ increases (Chung et al. 2013; Oakey et al. 2010). This is likely due to hydrodynamic interactions between particles that help them reach their equilibrium positions (Oakey et al. 2010).

For channels with curves or variable cross-sections, such as the μHammer's inlet focusing channel, the locations and widths of focusing streams are much harder to predict. These geometries introduce secondary flows that interact with the inertial lift forces to create new equilibrium locations (Di Carlo et al. 2007). The magnitude of this interaction is described by the Dean number, De, which scales Re to account for the varying curvature of the channel:

$$De = Re \cdot f\left(D_h, r_{eff}\right),$$

where f is a function of D_h and the channel's effective radius of curvature, r_{eff}. Collectively, these dependencies indicate that flow velocity, particle size, particle concentration, and buffer viscosity (which in turn depends on temperature) will all affect the trajectory of particles flowing through our device.

2.3 Flow focusing in the μHammer

In the context of the μHammer, cells or other particles passing through its microfluidic channels experience a combination of inertial forces, viscous forces, and secondary flows. These interactions focus the particles into predictable regions of the channels prior to impact. As described in Section 2.1, particles initially flow through a focusing channel of varying cross-section before entering the μHammer chip. This channel geometry introduces secondary flows that interact with the forces typically experienced in rectangular channels, directing particles into one of two streams vertically oriented on the same side of the focusing channel (Fig. 2b). As particles transition into the rectangular μHammer channel, the focused streams maintain the same orientation. However, due to the change in aspect ratio, the equilibrium locations shift and the focused streams begin to migrate toward each other (Fig. 2c). Since the μHammer channel is relatively short (~350 μm), streams may or may not converge depending on the L_{min} for those experimental conditions.

Achieving and maintaining focused streams in the μHammer channel is important, since the fluid velocity in a rectangular channel decays parabolically from its center during Poiseuille flow (Lee et al. 2006; White and Corfield 2006). The μHammer meets the conditions of a Poiseuille flow, with an incompressible fluid as the buffer, a low Re on the order of 10 to 100 (ensuring laminar flow), and L (~350 μm) much greater than D_h (~30 μm). Thus, by limiting the lateral movement of particles as they travel through the μHammer and by making their path more consistent, inertial focusing minimizes the magnitude of velocity changes during transit. Focusing also constrains the particles to a narrow window of distances from the side of the channel, which makes the initial contact point between the μHammer impact face and the particles more uniform. Given this improved consistency in both particle velocity and location, it is clear that flow focusing is a powerful tool for optimizing the timing and ultimately the throughput of our device.

2.4 Imaging bead impacts

In order to characterize the μHammer's timing, we captured images of 6-μm-diameter Polybead® microbeads (Polysciences, Inc., USA) as they were held in compression following impact. These beads were suspended in buffer at the appropriate concentration to enable the detection and impact of 300 ± 50 beads/s (2.8×10^5 beads/mL for slow bead

velocity, u_S, and 1.4×10^5 beads/mL for high bead velocity, u_F). They were then strained with a 10-μm CellTrics filter (Sysmex Partec, Germany) and loaded into the μHammer cartridge. The beads were pressure-driven through the device and timed using backscatter signals generated with the 405- and 488-nm-wavelength lasers, as described in Section 2.1. Once the beads were timed and impacted by the μHammer, they were held in compression for 200 μs and imaged by a Ximea MQ003MG-CM high-speed camera (Ximea, Germany). These images were taken at a rate of 10 Hz to gather data from a representative fraction of the total impacted bead population. Using image analysis software (ImageJ Version 1.50i, public domain), we classified the captured beads according to their position along the impact face. Beads found within 7 μm of either pincer were labeled "burst," while beads outside of these zones near the center of the impact face were labeled "centered." If no bead was found in the image, we applied the label "missing."

This assay was first performed with different t_{AC} (post-arrival closure time) values for both u_S and u_F bead velocities, all at 37 °C with an x_{LH} (laser-hammer separation distance) of 80 μm. The results were used to determine the optimal t_{AC} values for both u_S and u_F settings based on the percentage of centered bead impacts. To determine how the measured bead displacement across the μHammer impact face (as a function of t_{AC}) compares to the expected bead displacement (as a function of u), we only imaged and analyzed beads within a small range of t_{LL} (intra-laser transit time) values in this assay (42 μs < t_{LL} < 45 μs for u_S, 23 μs < t_{LL} < 26 μs for u_F). For each t_{AC} value, 400 images were collected with the same μHammer device and analyzed. For all bead imaging, data was collected over the course of approximately one minute for each experimental replicate.

Using the optimal t_{AC} values that resulted in the highest percentage of centered bead impacts, we then quantified the percentage of beads that were centered and missing as a function of bead velocity (u_F vs u_S), temperature (8 vs 37 °C), and laser-hammer separation distance (80 vs 60 μm). For each combination of settings tested, at least 5 replicates of 500 images were collected. Each replicate was obtained using a unique device.

To determine the effects of throughput on μHammer timing, we increased the concentration of beads first to 5.6×10^5 beads/mL and then to 1.1×10^6 beads/mL (corresponding to volume fractions, φ, of 6.0×10^{-5} and 1.2×10^{-4}). We then impacted them with our benchmark settings (37 °C, u_S, 60-μm x_{LH}) at throughput values of 600 ± 50 beads/s and 1200 ± 50 beads/s, respectively. For the 600 beads/s group, four replicates of 500 images were gathered with different devices. Only one dataset was acquired for the 1200 beads/s group, since at this concentration the beads tended to accumulate between the Ni–Fe poles and prevent actuation.

2.5 Measuring bead transit times and velocity

In order to investigate the effects of temperature and average bead velocity on the μHammer's flow profile, we suspended 6-μm beads in buffer at the appropriate concentration for a throughput of 300 ± 50 beads/s (as described in Section 2.4), then flowed them through the μHammer device at a controlled average velocity (u_F or u_S). We did this at both 8 °C and 37 °C while measuring the transit time between lasers, t_{LL}, of each bead. The solenoid was never actuated, allowing the beads to pass through the device unimpacted. For each of these experimental groups, data were collected over the course of approximately 0.5 min with a single device until a total of 10,000 beads were measured.

In subsequent experiments, we repeated the same assay with different experimental conditions. First, we added BSA at 5% *w*/*v* to increase the viscosity of the buffer solution and measured the t_{LL} of beads flowing through the device at 37 °C with u_F settings. Next, we replaced the 6-μm beads with 7.5-μm SPHERO™ polystyrene beads (Spherotech, Inc., USA) and then with 10-μm Polybead® polystyrene beads (Polysciences, Inc., USA) to repeat the assay, also at 37 °C with u_F bead velocity. Finally, we increased the concentration of 6-μm beads to achieve a throughput of 600 beads/s and measured the t_{LL} of each bead at 37 °C with u_S bead velocity.

To further investigate the effects of throughput on timing efficacy, we measured the bead velocity, u, as a function of time after the previous actuation, t_{SD}. Since the t_{LL} values for low t_{SD} were too large to measure accurately, we instead measured the full-width half-maximum travel time, t_{FWHM}, across the final detecting laser. This assay was performed using our benchmark settings (37 °C, u_S, 60-μm x_{LH}) at a throughput of 600 beads/s. We gathered data from a total of 60,000 beads over the course of approximately 2 min. A least-squares linear regression was fit to a t_{LL} vs t_{FWHM} plot of the data, which was then used to transform from t_{FWHM} to t_{LL} and ultimately to the bead velocity, u.

2.6 Statistical analysis

All statistical analysis was performed with GraphPad Prism (version 8.4.1). Where indicated, Savitsky-Golay smoothing was applied using a sixth-order polynomial. No smoothing or other statistical treatment was applied to datasets reporting quantitative values. Comparisons of 3 or more groups were performed via two-way ANOVA with Tukey's multiple comparisons test. Comparisons of two groups were performed via unpaired *t*-test, $\alpha = 0.05$.

3 Results

3.1 Timing quantification and optimization

The most direct way to characterize the μHammer's timing would be to image biological cells as they are held in compression following impact. However, cells are optically transparent and highly deformable, and thus are difficult to image clearly through the depth of the channel. To obtain sharper images that are easier to analyze, we used 6-μm-diameter polystyrene beads instead. This particular bead size was chosen because beads larger than 6 μm become wedged between the tapered Ni–Fe poles and prevent actuation. Only rigid particles like polystyrene beads experience this form of clogging, since larger viscoelastic particles like cells can easily pass between the Ni–Fe poles unperturbed. Furthermore, the 6-μm beads were chosen because they are larger than the 4-μm final gap distance under full compression, x_G. As a result, the μHammer pincers do not close all the way but are held 1 to 2 μm from the channel wall by the rigid beads (Fig. 3a), ensuring that the beads are immobilized between the μHammer face and the channel wall during compression. This allows us to determine the position along the μHammer face where the beads were impacted. Beads found within 7 μm of either pincer were labeled "burst," since cells larger than 14 μm impacted within these zones are likely burst (Patterson et al. 2019). Beads outside these zones near the center of the impact face were labeled "centered," while images with no bead visibly present were labeled "missing."

In order to determine the optimal t_{AC} values that result in the highest percentage of centered beads, we impacted beads with different t_{AC} values for both u_S and u_F bead-velocity settings. As shown in Fig. 3b, three t_{AC} values resulted in finding a majority of beads in the centered region (orange, with $t_{AC} = 3$ μs being optimal) for u_S settings. By comparison, five t_{AC} values resulted in a majority of beads being found in the burst region (blue). This indicates there is a preference for the beads to end up along the edges of the impact face near the pincers, which may be due to the displacement of fluid toward the edges of the μHammer during actuation. Furthermore, given the measured bead velocity, u (1.1 to 1.2 m/s), it should take ~24 μs for the beads to "walk" across the width of the μHammer impact face, x_{HF} (28 μm). However, it only took a 7 μs change in t_{AC} values for the majority of beads to traverse this distance (Fig. 3b). This indicates that the average bead velocity may increase while the μHammer actuates. A similar trend was found for u_F settings (Fig. 3c), which had only two t_{AC} values that resulted in a majority of centered beads and two values that resulted in a majority of burst beads. This decrease in both total and centered t_{AC} values is likely due to the higher average bead velocity compared to u_S settings, which reduces the amount of time beads are in the impact region and thus decreases the safety factor for error in timing.

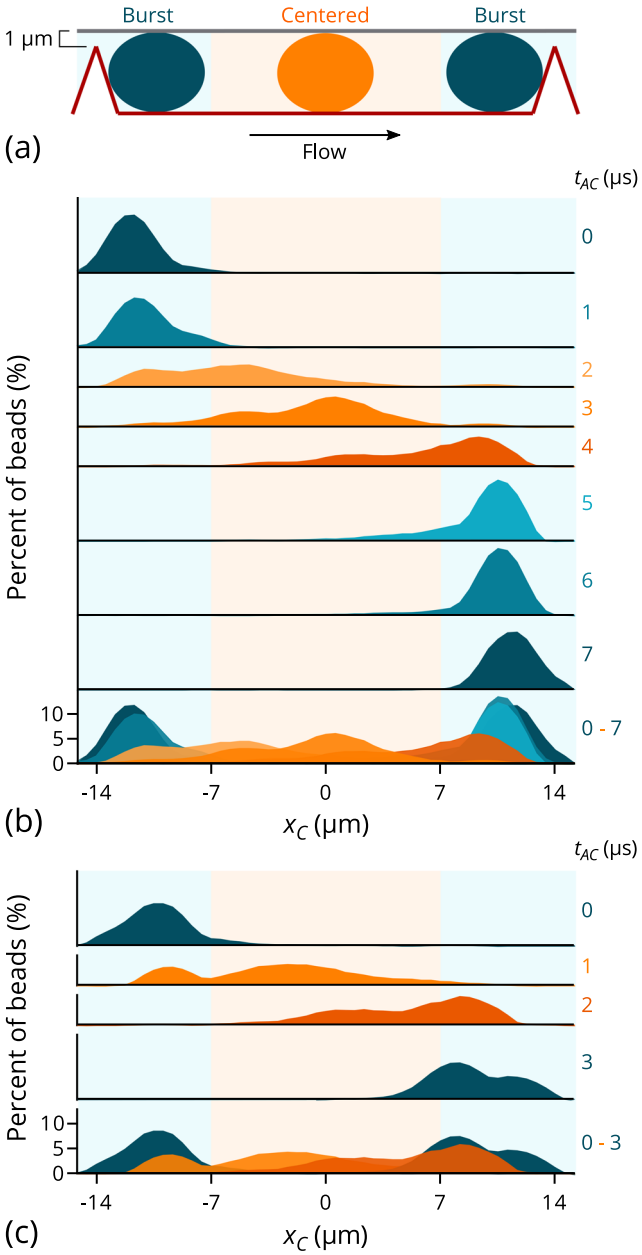

Fig. 3 Slow bead-velocity settings have a greater safety factor for error than fast bead-velocity settings. **a** Schematic of μHammer face while impacting beads. μHammer impact face (shown in red outline) scaled to match x-axis of panels b and c. Beads shown being impacted in the burst and centered regions, shaded blue and orange, respectively. Distance between channel wall and μHammer pincers labeled. Flow is from left to right across μHammer face. **b** Histograms of bead-center separation distance, x_C, for slow bead velocity, u_S, as a function of post-arrival closure time, t_{AC}. Each histogram corresponds to a different t_{AC} value. **c** Histograms of x_C for fast bead velocity, u_F, as a function of t_{AC}. In all cases, the two outer quadrants (7 μm < $|x_C|$ < 14 μm) correspond to the "burst" region, and the two inner quadrants ($|x_C|$ < 7 μm) correspond to the "centered" region. Blue histograms correspond to t_{AC} values that result in the majority of beads being impacted in the burst region, while orange histograms correspond to t_{AC} values that result in the majority of beads being impacted in the centered region. Only t_{AC} values that result in less than 50% of beads being labeled as missing are shown. $N = 400$ images analyzed for each t_{AC} value. Histograms were created with a bin width of 0.6 μm and were lightly smoothed with a Savitsky-Golay filter averaging 4 values on each side

In order to determine how temperature and velocity affect the performance of the μHammer, we quantified μHammer impacts under different conditions with our optimal t_{AC} values as shown in Fig. 4a. These results demonstrate that there was no significant difference in the percentage of centered and missing beads between fast bead-velocity settings, u_F, and slow bead-velocity settings, u_S, at 8 °C. However, increasing the temperature to 37 °C led to an increase in centered impacts with u_S settings and a significant decrease with u_F settings.

In Fig. 4b, we see that decreasing the laser-hammer separation distance, x_{LH}, from 80 μm to 60 μm significantly increased the percentage of centered impacts. This indicates that at least some of the burst and missing beads are the result of t_{LL} (laser transit time) measurement errors or changes in bead velocity between laser detection and solenoid activation. When either of these occur, the bead arrives in the impact region at a different time than predicted. This increases the likelihood that the bead will be burst or even missed completely. By decreasing x_{LH}, we decrease the distance between the measurement and impact areas, limiting the magnitude of these timing errors and subsequently increasing the percentage of centered impacts.

Finally, to determine the effect of concentration on device performance, we analyzed μHammer impacts while running at increasing concentrations of 5.6×10^5 beads/mL and then 1.1×10^6 beads/mL (corresponding to throughput values of 600 beads/s and 1200 beads/s). These results were compared to those obtained previously at a concentration of 2.8×10^5 beads/mL (300 beads/s). As shown in Fig. 4c, the percentage of centered beads decreased as the concentration increased. The highest percentage of centered beads (~75%) was achieved with the lowest throughput tested (300 beads/s). This translates to an effective impact frequency, ω_{eff}, of 225 centered beads/s. However, the highest ω_{eff} (360 centered beads/s) of the settings we tested that resulted in minimal missing beads (< 5%) was achieved with a throughput of 600 beads/s. Under these settings, the higher overall throughput compensates for the decreased percentage of centered beads (~60%), thereby maximizing ω_{eff}.

3.2 Sensitivity to Reynolds number

As discussed in Section 2.3, the focusing element positioned before the μHammer channel is designed to focus the beads into one of two streams (Fig. 2b). These streams are stacked vertically on the side of the channel nearest to the impact face at rest. Once the beads enter the μHammer channel and flow through it, the streams begin to shift towards each other as shown in Fig. 2c. However, the predicted distance required for convergence of these streams, L_{min}, is approximately 1000 μm for u_F, 37 °C settings (and even higher for the other conditions tested) with 6-μm beads. Since the μHammer channel is only 350-μm long, this indicates that the streams will not converge. Instead, they remain as two vertically stacked streams on the same side of the channel, whose location can vary with Re_p. The system's Re_p value, in turn, depends on the maximum flow velocity, u_{max} (which we estimate to be equivalent to the maximum bead velocity), the dynamic viscosity, μ (which we estimate based on the temperature and BSA concentration of the buffer solution using the relationship generated by Monkos (1996)), and the bead diameter, a. These relationships suggest that the changes in impact efficacy illustrated in Fig. 4a may be due to changes in the focusing profile.

In order to uncover the mechanism behind these changes in device performance, we investigated how different experimental settings influenced the flow of beads through the μHammer. We explored this by measuring the laser transit time, t_{LL}, of each bead as it passed through our device. As shown in Fig. 5a, the t_{LL} values for u_S bead-velocity settings at both 8 °C and 37 °C were grouped into two distinct peaks. In our images of bead impacts, the beads in the peak with higher t_{LL} values were in a focal plane closer to the top of the channel than beads in the peak with lower t_{LL} values.

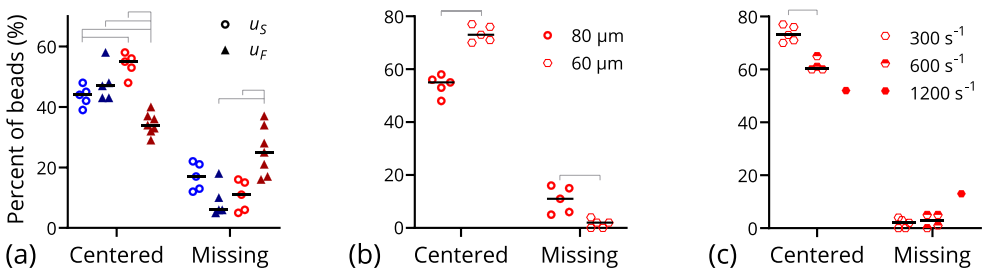

Fig. 4 Efficacy of μHammer timing varies with temperature, bead velocity, laser-hammer separation distance, and throughput. **a** Percentage of centered and missing beads as a function of temperature and bead velocity. Four different combinations of parameters were tested: 8 °C temperature in blue, 37 °C in red, u_S bead velocity as open circles, and u_F as filled triangles. **b** Percentage of centered and missing beads as a function of laser-hammer separation distance, x_{LH}. Data for 80-μm x_{LH}, u_S bead-velocity settings duplicated from panel a for reference. **c** Percentage of centered and missing beads as a function of impact frequency. Data for 300 bead/s throughput, 60-μm x_{LH} settings duplicated from panel b for reference. $N = 500$ images analyzed for each experimental replicate. Black line depicts average of replicates for each group, gray brackets connecting two groups indicate statistical difference ($p < 0.01$). Factors tested by two-way ANOVA in panel a were temperature and bead velocity

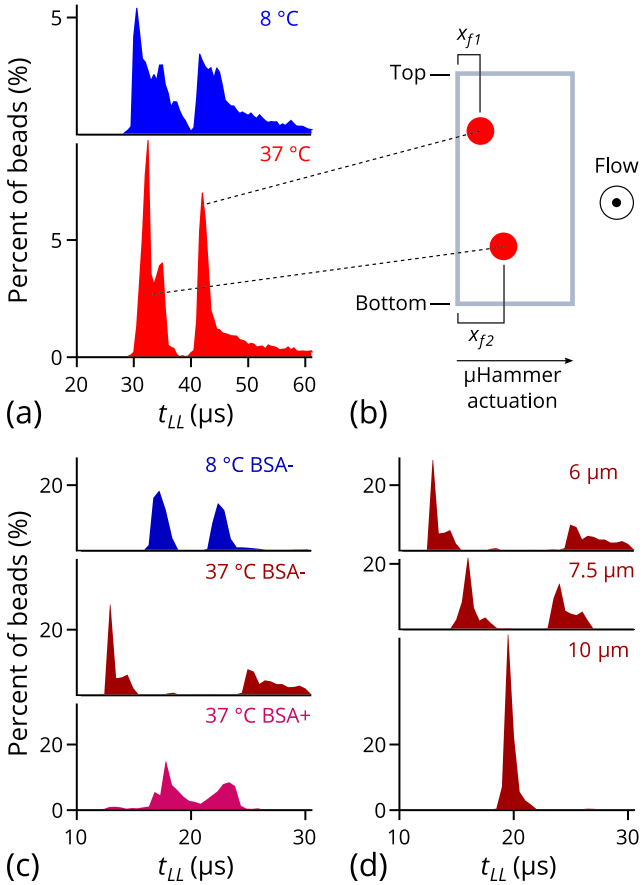

Fig. 5 μHammer flow profile varies with changes in the particle Reynolds number, Re_p. **a** Histograms of the laser transit times, t_{LL}, for u_S bead-velocity settings as a function of temperature. **b** Slice of μHammer channel with approximate locations of the two focused streams. Top and bottom of channel are marked, as well as direction of μHammer actuation across channel. Flow direction is out of page. Distances between top / bottom stream and side of μHammer channel are marked x_{f1} and x_{f2}, respectively. Note that $x_{f1} < x_{f2}$. Distances of streams from top and bottom walls of the channel can also vary. **c** Histograms of t_{LL} for u_F settings as a function of temperature and viscosity. **d** Histograms of t_{LL} for u_F, 37 °C settings as a function of bead size. 6-μm bead data duplicated from panel c for reference. $N = 10{,}000$ beads analyzed for each experimental condition. All t_{LL} histograms created with a 0.5-μs bin width

This suggests that these peaks each correspond to a separate stream with a different range of fluid velocities. Since the fluid velocity in the channel decays parabolically from the center, the peak with higher t_{LL} values and thus lower bead velocities likely corresponds to a stream that is closer to the channel wall than the other focused stream ($x_{f1} < x_{f2}$, Fig. 5b). Furthermore, Fig. 5a shows that the width of the transit-time peaks decreased when the temperature changed from 8 °C ($\mu =$ 1.3 mPa·s, $Re_p = 1.4$) to 37 °C ($\mu = 0.7$ mPa·s, $Re_p = 2.5$). This indicates that the width of the focused streams decreases with increased temperature for u_S settings, ultimately demonstrating an increase in focusing performance.

For u_F bead-velocity settings, on the other hand, the t_{LL} peaks and thus the bead streams were already tightly focused at 8 °C ($\mu = 1.3$ mPa·s, $Re_p = 2.4$, Fig. 5c). When the temperature increased to 37 °C ($\mu = 0.7$ mPa·s, $Re_p = 6.0$), the t_{LL} peaks shifted dramatically outward, widening the gap between them (Fig. 5c). This suggests that the slower stream focuses even closer to the wall as the temperature increases for u_F settings ($x_{f1,\ 37C} < x_{f1,\ 8C}$). When this occurs, the velocity of the slower stream decreases, while the velocity of the faster stream conversely increases in order to maintain the same average bead velocity, u_F. This hypothesis is supported by the fact that in straight channels, the equilibrium stream position gets closer to the channel wall with increasing Re (Di Carlo et al. 2007) and thus with decreasing viscosity.

Based on these results, we hypothesize that the relationship between temperature and buffer viscosity, μ, is the root cause of these differences in bead trajectory and stream focusing when the average bead velocity is held constant. To confirm this, we added BSA to the buffer solution at 5% concentration (w/v). This addition slightly increased μ to 0.9 mPa·s and Re_p to 3.8 at 37 °C with u_F settings, resulting in μ and Re_p values intermediate between their respective values at 8 °C and 37 °C. As shown in Fig. 5c, the t_{LL} profile for this condition was also intermediate between the 8 °C and 37 °C profiles in the absence of BSA. This indicates that μ is indeed the driving force behind changes in focusing with temperature and is thus a useful tool that can be used to fine-tune the focusing profile of our device.

Although we could not impact beads larger than 6 μm without clogging the device, we did gather information on the trajectories of these larger beads as they flow through the μHammer. The effect of bead diameter, a, on t_{LL} is shown in Fig. 5d. The t_{LL} peaks of the 7.5-μm beads ($Re_p = 8.5$) were shifted closer together compared to the peaks of the 6-μm beads ($Re_p = 6.0$), while the 10-μm beads ($Re_p = 12.2$) had only one t_{LL} peak. In these cases, it seems probable that the edge of the faster stream at the bottom of the channel moves closer to the wall as the bead size increases. This continues until the bead size reaches 10 μm, at which point the stream at the bottom of the channel is the same distance from the wall as the stream at the top of the channel ($x_{f1} = x_{f2}$). The two streams may even converge under these conditions, since the predicted L_{min} is only 300 μm for 10 μm beads at 37 °C with u_F settings. Thus, the beads may travel a sufficient distance along the length of the μHammer channel to reach their equilibrium positions in this scenario. Collectively, these results indicate that particle size, fluid velocity, and buffer viscosity are all crucial elements to consider when using the μHammer or any other microfluidic device where timing is important.

3.3 Sensitivity to bead concentration and throughput

As discussed in Section 2.2, concentration is another parameter that can affect the flow of beads through microfluidic channels. Beads are more likely to focus into their equilibrium

streams when the volume fraction, φ, of beads in solution is on the order of 1×10^{-3} or lower. The highest φ that we tested was 1×10^{-4} (for 6-μm beads at a concentration of 1.1×10^{6} beads/mL), indicating that these solutions fall in the region of volume fractions where increasing concentration can have a positive effect on bead focusing. This hypothesis is confirmed by the results in Fig. 6a, where the laser transit-time t_{LL} peaks narrowed in width and moved slightly closer together as the concentration increased from 2.8×10^{5} to 5.6×10^{5} beads/mL (corresponding to throughput values of 300 and 600 bead/s, respectively).

To further explore the effect of throughput on device performance, we analyzed how actuation affects the flow profile of beads through the device. We did this by tracking the bead velocity, u, as a function of time since the last actuation, t_{SD}, as shown in Fig. 6b. In this plot, we only show the highest u value for each t_{SD}, likely corresponding to beads travelling down the middle of the channel where the flow velocity is highest. This allows us to rule out interactions with the sidewalls as the cause for any changes in velocity. Fig. 6b shows that u increased immediately after actuation began ($t_{SD} = 0$ μs) until the μHammer reached full actuation ($t_{SD} = 18$ μs). It then quickly dropped by ~90%, after which it slowly recovered until it returned to steady-state ($t_{SD} \approx 600$ μs).

This dynamic bead-velocity profile reflects changes in the fluidic path through the device during actuation. When the μHammer begins to actuate, it blocks a portion of the channel and thus narrows the width of the fluidic path. Once the μHammer reaches the other side of the channel, it diverts all fluid to the waste via during the hold time of compression. It then returns to rest, allowing the fluid to flow normally into the output via until the next actuation. These sudden changes to both the fluidic resistance and the fluidic path cause the flow velocity to change dramatically, then slowly recover as the flow profile returns to steady-state.

The probability that such a dramatic change in velocity will occur to any given bead is directly related to throughput. As the throughput increases, the average time between consecutive bead detections decreases. This in turn results in an increased percentage of beads (5% to 10% at 300 beads/s, 20% at 600 beads/s, 40% at 1200 beads/s) with low t_{SD} values (< 600 μs). Beads detected in this low t_{SD} region are accelerating and thus are difficult to time. As a result, minimizing the number of beads present in this region will maximize the percentage of centered bead impacts, indicating the importance of considering both particle concentration and throughput in experimental design for microfluidic devices.

4 Discussion

In this work, we demonstrate that the focusing ability and thus the impact performance of the μHammer are strongly influenced by the parameters encapsulated by the particle Reynolds number, Re_p. These parameters include temperature, buffer viscosity, particle velocity, and particle size. As shown in Fig. 5a, the focusing performance of the device increases for u_S bead-velocity settings when the temperature changes from 8 °C ($Re_p = 1.4$) to 37 °C ($Re_p = 2.5$). In Fig. 4a, we find that the percentage of centered bead impacts at 37 °C was significantly higher than at 8 °C for u_S settings, demonstrating the benefit of this increased focusing ability. Our results also suggest that particle size can have a similar effect on impact performance, since the focusing ability of the μHammer increases with bead size (Fig. 5d).

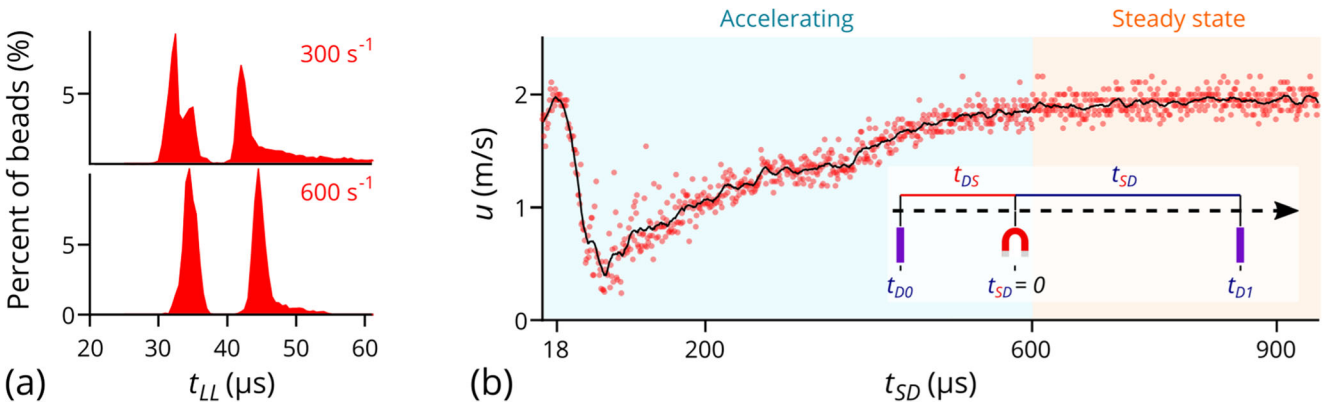

Fig. 6 μHammer flow profile varies with bead concentration and throughput. **a** Histogram of laser transit time, t_{LL}, as a function of throughput for u_S, 37 °C settings. 300 beads/s throughput data duplicated from Fig. 5a for reference. $N = 10{,}000$ beads analyzed for each experimental condition. **b** Bead velocity, u, as a function of time after the μHammer last actuated, t_{SD}. Inset illustrates relationship between the time bead 0 is detected (t_{D0}), the time solenoid is activated to impact bead 0 ($t_{SD} = 0$), and the time bead 1 (whose velocity is plotted in this panel) is detected (t_{D1}). Only the maximum u value measured for each t_{SD} value is shown, taken from a total of 60,000 measurements across all t_{SD} values. The μHammer begins to actuate at 0 μs, completes actuation at 18 μs, and begins to return to rest at 200 μs. Accelerating ($t_{SD} < 600$ μs) and steady-state ($t_{SD} > 600$ μs) velocity regions marked on chart with blue and orange backgrounds, respectively. Black line depicts data points smoothed with a Savitsky-Golay filter averaging 10 points on each side

While focusing performance is a powerful tool for optimizing impact efficacy, other phenomena influenced by the same parameters that define Re_p must also be considered. For example, the bead streams at 8 °C with u_F bead-velocity settings ($Re_p = 2.4$, Fig. 5c) and at 37 °C with u_S settings ($Re_p = 2.5$, Fig. 5a) are both tightly focused, but fewer of the bead impacts were centered with u_F settings than with u_S settings (Fig. 4a). This is likely due to the higher average bead velocity of the u_F settings, which decreases the safety factor for error in overall timing. Furthermore, when the temperature increases from 8 °C ($\mu = 1.3$ mPa·s, $Re_p = 2.4$) to 37 °C ($\mu = 0.7$ mPa·s, $Re_p = 6.0$) for u_F settings, the focusing profile shifts (Fig. 5c). This causes the beads travelling through the stream furthest from the wall (x_{f2}) to move too fast for the μHammer to impact properly, decreasing the percentage of centered impacts (Fig. 4a). To overcome this unwanted shift in bead trajectory through the device, our results indicate that buffer viscosity, μ, can be adjusted independently of temperature by the addition of BSA, thereby restoring the desired flow profile (Fig. 5c) and impact efficacy.

In addition to the parameters encompassed by Re_p, bead concentration and throughput also influence the trajectory of beads through the device and thus affect its overall performance. Our results indicate that the focusing capabilities of the μHammer increase with concentration (Fig. 6a), in agreement with the findings of other studies (Chung et al. 2013; Oakey et al. 2010). However, the percentage of centered beads actually decreased with concentration (Fig. 4c) due to the negative effect of actuation on bead velocity (Fig. 6b). This is a function of throughput as opposed to concentration, since beads are only affected if they are detected soon after the previous μHammer actuation. When the throughput increases, the odds that each individual bead will undergo a dramatic change in velocity increases. This, in turn, decreases the percentage of properly timed and centered impacts. As a result, while the highest effective throughput, ω_{eff}, was achieved with a total throughput of 600 beads/s, the highest percentage of centered bead impacts was achieved with a throughput of 300 beads/s. This indicates that efforts to reduce the change in bead velocity with actuation could further increase ω_{eff}.

In order to minimize the detrimental effect of throughput and other phenomena on μHammer timing, our results suggest a number of design optimizations that could further improve the μHammer's performance. For example, we could alter the channel geometry to reduce changes in fluidic resistance during actuation. This would decrease the resulting fluidic acceleration, maximizing the percentage of centered impacts at higher throughput values. Furthermore, redesigning the channel geometry by increasing the width of the channel right before the impact face would decrease the fluid velocity in that region. In turn, the bead velocity would decrease as it passes through that region before impact, further increasing the safety factor for error in timing. Finally, to reduce the detrimental effect of measurement errors and bead-velocity changes on timing, the μHammer could be redesigned with a wider hit face ($x_{HF} > 28$ μm). This would expand the range of centered t_{AC} values and thereby increase the percentage of centered impacts.

Although geometric redesigns can be a useful tool to improve the performance of the μHammer and other microfluidic devices that rely on timing, such changes can be time-consuming, expensive, or even impossible to implement in certain systems. In the absence of any device-specific changes, we believe that our results provide a general framework for optimizing device performance immediately by simply adjusting the experimental parameters. For example, our results show that slow particles have a higher safety factor for error in timing than fast particles. However, reducing the average particle velocity could also decrease the focusing capability of the device, since it would lower Re_p. This tradeoff could be avoided by increasing the particle volume fraction, φ, which would help restore the focusing performance and thus maximize the effective impact frequency, ω_{eff}.

It is important to note that the experiments in this study were performed with spherical beads that are orders of magnitude stiffer than the biological cells our device is designed to impact (Young's modulus on the order of GPa for polystyrene versus ~kPa for cells) (Hiorns 2000; Luo et al. 2014). Although the deformability of cellular particles adds another degree of complexity, they still can be focused into equilibrium streams in microfluidic channels whose location depends on the ratio of inertial to viscous forces (Di Carlo et al. 2007; Hur et al. 2011; Ozkumur et al. 2013; Wang et al. 2015). Preliminary studies indicate that cells impacted by the μHammer exhibit the same timing characteristics that we demonstrate here using beads. In fact, the percent decrease in human leukemic K562 cells after impact with u_S, 8 °C settings reported in our previous work (Patterson et al. 2019) is roughly equal to the percentage of beads found in the burst region for the same settings described in this manuscript (Fig. 4a). This likely confirms that cells impacted in this region are burst as intended, ensuring the uniformity of impact parameters (Patterson et al. 2019). Furthermore, it demonstrates that beads are a useful tool that can approximate and even predict the μHammer's performance with biological cells.

5 Conclusions

In this work, we provide a case study for the design and analysis of microfluidic systems that rely on consistent particle trajectories and timing. A number of broadly used biomedical instruments exploit both these phenomena, the most prominent being microfluidic flow cytometers (Bhagat et al. 2010b; Oakey et al. 2010) and

cell sorters (Bhagat et al. 2010a; Foster et al. 2018). Other systems may not involve particles but still utilize flow focusing, with applications in the field of biomedicine ranging from drug delivery (Björnmalm et al. 2014) to tissue engineering (Oh et al. 2013), as well as applications across disparate fields such as wastewater treatment (Han et al. 2017) and materials manufacturing (Nunes et al. 2014). When parameters like temperature or particle size change in these systems, our results indicate that it is possible to maintain or even improve device performance by adjusting other parameters including viscosity and flow velocity. These changes can be implemented immediately, as opposed to more complex geometric redesigns which are often costly and time-consuming to execute, and in some cases are not even possible. The principles we describe in this manuscript provide a simple framework for optimizing any microfluidic device that is sensitive to its fluid and particle trajectories, enabling flexibility in experimental design without sacrificing efficacy and throughput.

Funding information This work was supported by the National Science Foundation with grants from the Division of Chemical, Bioengineering, Environmental, and Transport Systems (award number 1631656) and from the Division of Civil, Mechanical, and Manufacturing Innovation (award number 1254893).

Data availability Not applicable.

Compliance with ethical standards

Conflict of interest The authors declare that they have no personal or institutional conflict of interest.

Code availability Not applicable.

References

E.S. Asmolov, The inertial lift on a spherical particle in a plane Poiseuille flow at large channel Reynolds number. J. Fluid Mech. **381**, 63–87 (1999)

A.A.S. Bhagat, S.S. Kuntaegowdanahalli, I. Papautsky, Inertial microfluidics for continuous particle filtration and extraction. Microfluid. Nanofluid. **7**, 217–226 (2009)

A.A.S. Bhagat, H. Bow, H.W. Hou, S.J. Tan, J. Han, C.T. Lim, Microfluidics for cell separation. Med. Biol. Eng. Comput. **48**, 999–1014 (2010a)

A.A.S. Bhagat, S.S. Kuntaegowdanahalli, N. Kaval, C.J. Seliskar, I. Papautsky, Inertial microfluidics for sheath-less high-throughput flow cytometry. Biomed. Microdevices **12**, 187–195 (2010b)

M. Björnmalm, Y. Yan, F. Caruso, Engineering and evaluating drug delivery particles in microfluidic devices. J. Control. Release **190**, 139–149 (2014)

A.J. Chung, D. Pulido, J.C. Oka, H. Amini, M. Masaeli, D. Di Carlo, Microstructure-induced helical vortices allow single-stream and long-term inertial focusing. Lab Chip **13**, 2942–2949 (2013)

Y. Deng, S.P. Davis, F. Yang, K.S. Paulsen, M. Kumar, R. Sinnott DeVaux, X. Wang, D.S. Conklin, A. Oberai, J.I. Herschkowitz, Inertial microfluidic cell stretcher (iMCS): Fully automated, high-throughput, and near real-time cell mechanotyping. Small. **13**, 1700705 (2017)

D. Desmaële, M. Boukallel, S. Régnier, Actuation means for the mechanical stimulation of living cells via microelectromechanical systems: A critical review. J. Biomech. **44**, 1433–1446 (2011)

D. Di Carlo, Inertial microfluidics. Lab Chip **9**, 3038–3046 (2009)

D. Di Carlo, D. Irimia, R.G. Tompkins, M. Toner, Continuous inertial focusing, ordering, and separation of particles in microchannels. Proc. Nat. Acad. Sci. **104**, 18892–18897 (2007)

J.S. Foster, K. Shields, M.R. Hoonejani, "Particle manipulation system with out-of-plane channel and variable cross section focusing element," U.S. Patent 9 962 702 B2, May 8, 2018

D.R. Gossett, T. Henry, S.A. Lee, Y. Ying, A.G. Lindgren, O.O. Yang, J. Rao, A.T. Clark, D. Di Carlo, Hydrodynamic stretching of single cells for large population mechanical phenotyping. Proc. Nat. Acad. Sci. **109**, 7630–7635 (2012)

T. Han, L. Zhang, H. Xu, J. Xuan, Factory-on-chip: Modularised microfluidic reactors for continuous mass production of functional materials. Chem. Eng. J. **326**, 765–773 (2017)

R. Hiorns, *Polymer Handbook*, 4th edn. (John Wiley and Sons, New York, 2000)

K.J. Humphry, P.M. Kulkarni, D.A. Weitz, J.F. Morris, H.A. Stone, Axial and lateral particle ordering in finite Reynolds number channel flows. Phys. Fluids **22**, 081703 (2010)

S.C. Hur, N.K. Henderson-MacLennan, E.R. McCabe, D. Di Carlo, Deformability-based cell classification and enrichment using inertial microfluidics. Lab Chip **11**, 912–920 (2011)

S. Kahkeshani, H. Haddadi, D. Di Carlo, Preferred interparticle spacings in trains of particles in inertial microchannel flows. J. Fluid Mech. **786** (2016)

G.-B. Lee, C.-C. Chang, S.-B. Huang, R.-J. Yang, The hydrodynamic focusing effect inside rectangular microchannels. J. Micromechanics Microengineering. **16**, 1024 (2006)

D. Lee, S.M. Nam, J.-a. Kim, D. Di Carlo, W. Lee, Active control of inertial focusing positions and particle separations enabled by velocity profile tuning with coflow systems. Anal. Chem. **90**, 2902–2911 (2018)

A.M. Leshansky, A. Bransky, N. Korin, U. Dinnar, Tunable nonlinear viscoelastic "focusing" in a microfluidic device. Phys. Rev. Lett. **98**, 234501 (2007)

O. Loh, A. Vaziri, H.D. Espinosa, The potential of MEMS for advancing experiments and modeling in cell mechanics. Exp. Mech. **49**, 105–124 (2009)

Y. Luo, D. Chen, Y. Zhao, C. Wei, X. Zhao, W. Yue, R. Long, J. Wang, J. Chen, A constriction channel based microfluidic system enabling continuous characterization of cellular instantaneous Young's modulus. Sens. Actuators B: Chem. **202**, 1183–1189 (2014)

M. Masaeli, E. Sollier, H. Amini, W. Mao, K. Camacho, N. Doshi, S. Mitragotri, A. Alexeev, D. Di Carlo, Continuous inertial focusing and separation of particles by shape. Phys. Rev. X. **2**, 031017 (2012)

K. Monkos, Viscosity of bovine serum albumin aqueous solutions as a function of temperature and concentration. Int. J. Biol. Macromol. **18**, 61–68 (1996)

J.K. Nunes, C.Y. Wu, H. Amini, K. Owsley, D. Di Carlo, H.A. Stone, Fabricating shaped microfibers with inertial microfluidics. Adv. Mater. **26**, 3712–3717 (2014)

J. Oakey, R.W. Applegate Jr., E. Arellano, D.D. Carlo, S.W. Graves, M. Toner, Particle focusing in staged inertial microfluidic devices for flow cytometry. Anal. Chem. **82**, 3862–3867 (2010)

J. Oh, K. Kim, S.W. Won, C. Cha, A.K. Gaharwar, Š. Selimović, H. Bae, K.H. Lee, D.H. Lee, S.-H. Lee, Microfluidic fabrication of cell adhesive chitosan microtubes. Biomed. Microdevices **15**, 465–472 (2013)

E. Ozkumur, A.M. Shah, J.C. Ciciliano, B.L. Emmink, D.T. Miyamoto, E. Brachtel, M. Yu, P.-i. Chen, B. Morgan, J. Trautwein, Inertial focusing for tumor antigen–dependent and–independent sorting of rare circulating tumor cells. Sci. Transl. Med **5**, 179ra47 (2013)

L.H. Patterson, J.L. Walker, E. Rodriguez-Mesa, K. Shields, J.S. Foster, M.T. Valentine, A.M. Doyle, K.L. Foster, Investigating cellular response to impact with a microfluidic MEMS device. J. Microelectromech. Syst. (2019)

A.E. Reece, J. Oakey, Long-range forces affecting equilibrium inertial focusing behavior in straight high aspect ratio microfluidic channels. Phys. Fluids **28**, 043303 (2016)

T. Sun, H. Morgan, Single-cell microfluidic impedance cytometry: A review. Microfluid. Nanofluid. **8**, 423–443 (2010)

J.D. Tice, A.D. Lyon, R.F. Ismagilov, Effects of viscosity on droplet formation and mixing in microfluidic channels. Anal. Chim. Acta **507**, 73–77 (2004)

S. Wang, X. Huang, C. Yang, Mixing enhancement for high viscous fluids in a microfluidic chamber. Lab Chip **11**, 2081–2087 (2011)

X. Wang, M. Zandi, C.-C. Ho, N. Kaval, I. Papautsky, Single stream inertial focusing in a straight microchannel. Lab Chip **15**, 1812–1821 (2015)

M.E. Warkiani, A.K.P. Tay, B.L. Khoo, X. Xiaofeng, J. Han, C.T. Lim, Malaria detection using inertial microfluidics. Lab Chip **15**, 1101–1109 (2015)

F.M. White, I. Corfield, *Viscous Fluid Flow* (McGraw-Hill, New York, 2006)

J. Zhang, S. Yan, D. Yuan, G. Alici, N.-T. Nguyen, M.E. Warkiani, W. Li, Fundamentals and applications of inertial microfluidics: A review. Lab Chip **16**, 10–34 (2016)